

Multi-Label Annotation of Chest Abdomen Pelvis Computed Tomography Text Reports Using Deep Learning

Vincent M. D'Anniballe^{*,a} Fakrul I. Tushar^{*,a,b} Khrystyna Faryna,^{a,b} Songyue Han^{a,c},
Maciej A. Mazurowski^a, Geoffrey D. Rubin^a, Joseph Y. Lo^a

^aCarl E. Ravin Advanced Imaging Laboratories, Department of Radiology, Duke University School of Medicine, 2525 Erwin Rd. Ste. 302, Durham, USA, 27705

^bErasmus+ Joint Master In Medical Imaging and Applications, University of Girona, Girona, Spain

^cSchool of Software Engineering, South China University of Technology, Guangzhou, Guangdong

*These authors contributed equally to this work

Purpose: To develop a high throughput multi-label annotator for body Computed Tomography (CT) reports that can be applied to a variety of diseases, organs, and cases.

Approach: First, we used a dictionary approach to develop a rule-based algorithm (RBA) for extraction of disease labels from radiology text reports. We targeted three organ systems (lungs/pleura, liver/gallbladder, kidneys/ureters) with four diseases per system based on their prevalence in our dataset. To expand the algorithm beyond pre-defined keywords, an attention-guided recurrent neural network (RNN) was trained using the RBA-extracted labels to classify the reports as being positive for one or more diseases or normal for each organ system. Confounding effects on model performance were evaluated using random or pre-trained embedding as well as different sizes of training datasets. Performance was evaluated using the receiver operating characteristic (ROC) area under the curve (AUC) against 2,158 manually obtained labels.

Results: Our model extracted disease labels from 261,229 radiology reports of 112,501 unique subjects. Pre-trained models outperformed random embedding across all diseases. As the training dataset size was reduced, performance was robust except for a few diseases with relatively small number of cases. Pre-trained Classification AUCs achieved ≥ 0.96 for all five disease outcomes across all three organ systems.

Conclusions: Our label-extracting pipeline was able to encompass a variety of cases and diseases by generalizing beyond strict rules with exceptional accuracy. As a framework, this model can be easily adapted to enable automated labeling of hospital-scale medical data sets for training image-based disease classifiers.

Keywords: weak supervision, attention RNN, rule-based algorithm, natural language processing, Computed Tomography.

1 Introduction

Machine learning algorithms have demonstrated considerable potential as disease classifiers for medical images. However, the majority of algorithms are specialized for a single organ or disease making their utility narrow in scope. This limited scope is mainly attributed to a sparsity of training data, since curating datasets for image-based classifiers has traditionally relied on radiologist annotation of the disease or its sequelae. As an alternative to image-based labeling, automated extraction of disease labels from radiology report text has the potential to address this training data scarcity and to avoid human annotation efforts (1-4).

Rule-based algorithms (RBA) are a conventional method for mining report text that utilize simple logic based on pre-defined keywords or patterns. In a landmark study, Wang et al. (5) used a RBA to extract labels of 8 thorax diseases from 108,948 chest X-ray reports to effectively train an image-based disease classifier. Using a similar method for CT, Draelos et al. (6) demonstrated the broad applicability of RBA-obtained labels by mining the more complex reports associated with over 36,000 chest CT volumes to train a classifier for 83 chest abnormalities. However, a major limitation of RBAs is that their performance and scope is reliant on the completeness of dictionaries containing pre-defined keywords. Furthermore, the radiologist's interpretation that accompanies a CT is usually composed in a free or semi-structured text form, rendering the extraction of disease labels using simple logical rules a nontrivial task (7).

To improve the utility of RBAs, extracted labels can then be used to train neural networks that deviate from strict rules by learning salient semantic features, a form of natural language processing (NLP) (8, 9). For example, Steinkamp et al. (10) trained a recurrent neural network (RNN) to classify disease in pathology reports written in unseen formats, suggesting the network had learned a generalizable encoding of the semantics. Building upon this NLP approach, Yuan et

al. (11) combined a pre-trained word embedding model with a deep learning-based sentence encoder to classify pulmonary nodules in a diverse set of radiology reports from different universities. While promising, it is often difficult to determine which semantic or structural features of the reports that the model perceives as most salient. To improve the interpretability of NLP-based classifiers, an attention-guided RNN (12) can be used to project the attention vector onto report text (13), allowing the user to visualize the words that a model is giving the most weight to when classifying an abnormality.

In this study, we propose a framework for automated, multi-disease label extraction of body CT reports based on an attention-guided RNN trained on RBA extracted labels. The RNN was trained to classify the lungs/pleura, liver/gallbladder, kidneys/ureters as being positive for one or more of four different diseases per system or normal. Although there has been extensive work in radiology report labeling, to our knowledge, there are no related works that demonstrate the utility of an RBA to train a deep learning-based NLP disease classifier in such a breadth of organ systems, diseases, and body CT reports.

This study is a considerable expansion of our previous studies (14, 15) and the main contributions are threefold:

- 1) To further refine our RBA to meet the challenges of free-text narration in radiology CT reports.
- 2) To broaden the utility of our extracted labels by training an attention-guided RNN to perform multi-label disease classification of CT reports.
- 3) To determine alternative factors that influence disease classification performance including random vs. pre-trained embedding and different sizes of training datasets.

2 Materials and Methods

In this section, we first describe the dataset that was used. Then, we outline the development processes of our RBA and the subsequent addition of an attention-guided RNN to enable multi-label classification of radiology reports. Figure 1 displays the overall workflow of this paper.

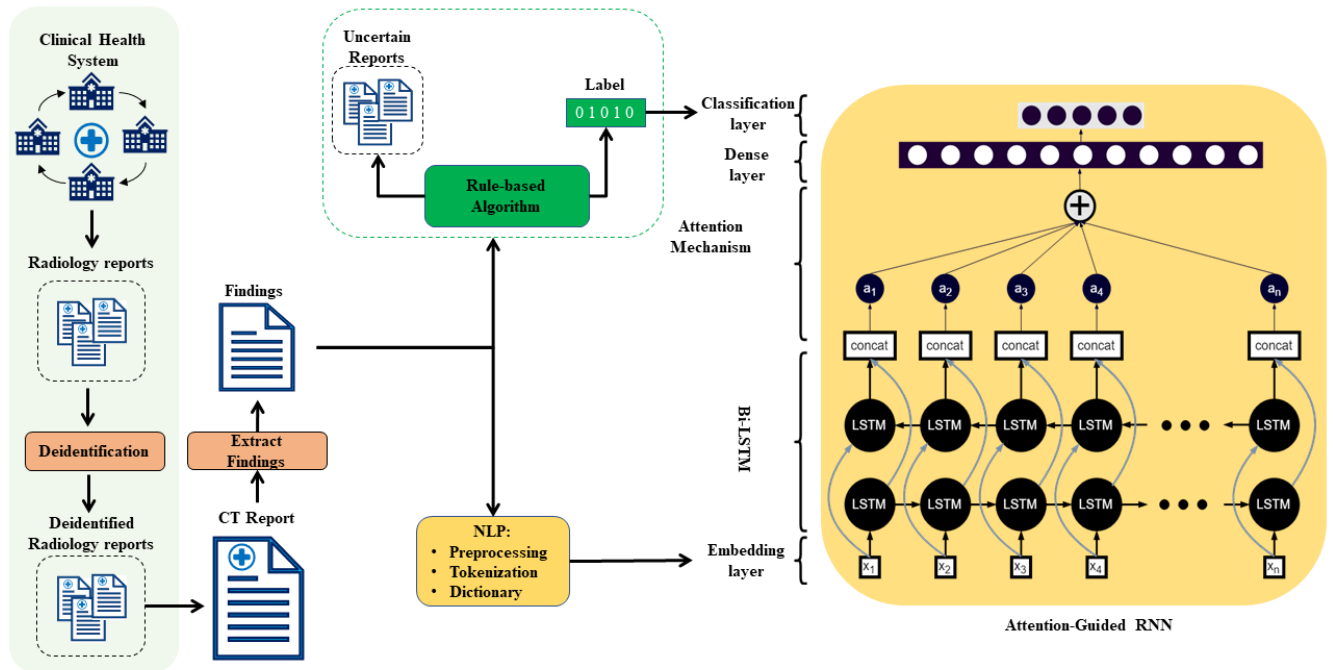


Fig. 1 Complete workflow. Radiology reports extracted from our health system were deidentified and the findings section was isolated. The reports were analyzed by an RBA and an attention-guided RNN to classify radiology reports for 5 different outcomes per organ system.

2.1 Dataset

A total of 261,229 chest, abdomen, pelvis structured CT reports of 112,501 unique subjects between the years 2012 to 2017 were extracted from the health system of our institution with IRB approval and deidentified. A representative example of a radiology CT report is shown in Figure

2, which contains protocol, indication, technique, findings, and impression sections. The distribution of CT protocols is shown in Figure 3.

Protocol: CT Chest without IV Contrast CT Abdomen and Pelvis without IV Contrast

Indication: C61 Malignant neoplasm of prostate (HCC), C79.51 Secondary malignant neoplasm of bone (HCC), Z00.6 Encounter for examination for normal comparison and control in clinical research program, staging

Technique: CT imaging of the chest, abdomen, and pelvis was performed without intravenous contrast. Coronal reformatted images were generated and reviewed. 3-D maximum intensity projection (MIP) reconstructions were performed of the chest to potentially increase study sensitivity.

Findings: Evaluation of the solid organs in the abdomen and pelvis is limited by the lack of IV contrast. Chest: Thyroid is unremarkable. Aortic atherosclerosis. Aorta is nonaneurysmal. Pulmonary artery is nonaneurysmal. Heart is normal in size. No pericardial effusion. Mild diffuse thickening of the thoracic esophageal wall. No axillary, mediastinal or hilar adenopathy. Coronary atherosclerosis. Small, stable nodes in the AP window. Central airways are patent. Basilar atelectasis. No focal pulmonary consolidation. No definite pulmonary nodule. Abdomen and pelvis: Liver contour is smooth. Gallbladder is unremarkable. The spleen, adrenal glands are normal. Pancreas is mildly fatty replaced. Mild bilateral perinephric stranding. Nonobstructive right renal stone in the inferior pole. No hydronephrosis. Mild stranding is seen around the distal left ureter. Aorta is nonaneurysmal. Diffuse aortoiliac atherosclerotic changes. Stomach is nondilated. Small bowel is nondilated. The appendix is normal. Bladder is unremarkable. The prostate is within normal limits of size. No free air. No free fluid. Adjacent to the distal rectum is a soft tissue nodule measuring 1.2 x 1.5 cm, unchanged from prior exam, and measures fluid density. Possibly small retroperitoneal extension of free fluid. Diffuse sclerotic osseous metastatic disease involving right femur, right and midline sacrum. Possibly L5 vertebral body. Sclerotic osseous lesions appear similar in distribution to prior exam.

Impression: 1. Stable osseous metastatic disease without significant interval change from September XXX, 2016. 2. No evidence of solid organ metastatic disease in the chest, abdomen or pelvis. Electronically Reviewed by: XXX, MD Electronically Reviewed on: XXX I have reviewed the images and concur with the above findings. Electronically Signed by: XXX, MD Electronically Signed on: XXX

Fig. 2 Representative example of a CT radiology report within our dataset.

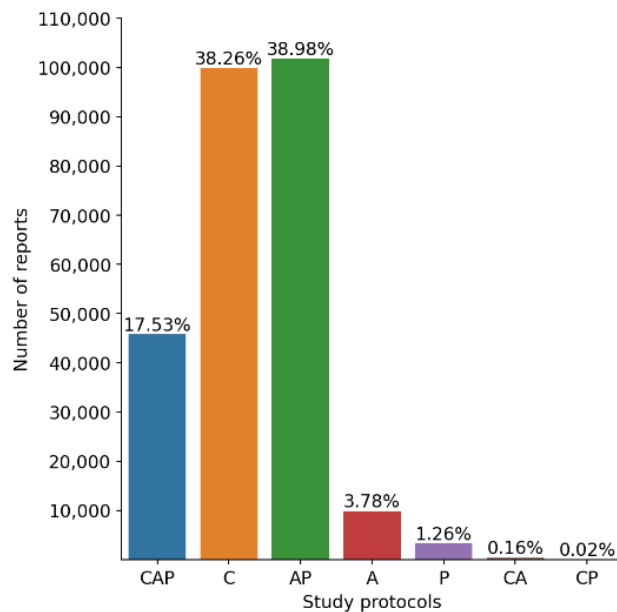


Fig. 3 Frequency of CT protocols in our dataset. CAP= chest abdomen pelvis, C=chest, AP=abdomen-pelvis, A=abdomen, P=pelvis, CA=chest-abdomen, CP=chest-pelvis

2.2 Rule-Based Algorithm (RBA)

The RBA was limited to the findings section of each CT report to minimize the influence of biasing information referenced in other sections and to ensure that the automated annotation reflects image information in the current exam (e.g., indication for exam, patient history, technique factors, and comparison with priors). For example, the impression section could describe a diagnosis based on patient history that could not be made using solely image-based information. In order to select target disease and organ keywords for the RBA dictionary, we computed term frequency–inverse document frequency (TF-IDF) (16) on the findings section of a representative batch of radiology reports. Informed by the prevalence of organ and disease keywords, we intentionally selected three organ systems and four findings for each organ, such that the labels varied widely in location, appearance, and disease manifestations. The three organ systems were the lungs/pleura, liver/gallbladder, and kidneys/ureters. For lungs/pleura, the four findings selected were atelectasis, nodule/mass, emphysema, and effusion. For liver/gallbladder; stone, lesion, dilation, and fatty liver. For kidneys/ureters; stone, lesion, atrophy, and cyst.

A board-certified radiologist (G.D.R.) provided guidance to define the TF-IDF terms into several categories, specifically:

- a) single-organ descriptors specific to each organ, e.g., pleural effusion or steatosis,
- b) multi-organ descriptors applicable to numerous organs, e.g., nodule or stone,
- c) negation terms indicating absence of disease, e.g., no or without,
- d) other terms describing confounding conditions, e.g., however, OR
- e) normal terms describing normal anatomy, e.g., unremarkable.

Appendix 1 displays the dictionary terms and their descriptor type for each organ system. The dictionary used in this study was substantially refined and expanded from our previous study (14)

by adding more terms and introducing wild-card entries to tackle misspellings or grammatical errors.

Figure 4 displays an overview of the RBA's flowchart and logic. After the dictionary was refined, all numbers and punctuation were removed from each report and the text was converted to lowercase and tokenized. In summary, the RBA was deployed on each sentence, and the number of potential diseases was counted first using the logic for the multi-organ descriptor and then the single-organ descriptor. If no potential diseases were detected, then the normal descriptor logic was finally applied to verify normality. This process was repeated for each organ system and disease outcome, allowing a report to be positive for one or more diseases or normal. Note that in this study an organ was defined as normal not only by excluding the four diseases studied but also in the absence of dozens of diseases that were not otherwise analyzed, as shown in Appendix 1. If the RBA failed to categorize the report definitively as positive for disease or normal (e.g., there was no mention of the organ system), then the report was labeled as uncertain and was not included in this study.

Upon manual review, we observed that many reports were incorrectly labeled as normal due to excessively long sentences, which were either complex sentences with multiple clauses or fused together due to grammatical errors (e.g., missing periods). Such sentences were impractical to analyze, so each report sentence was subject to a length criterion threshold for the normal outcome, another feature which made this RBA noticeably different from previous implementations.

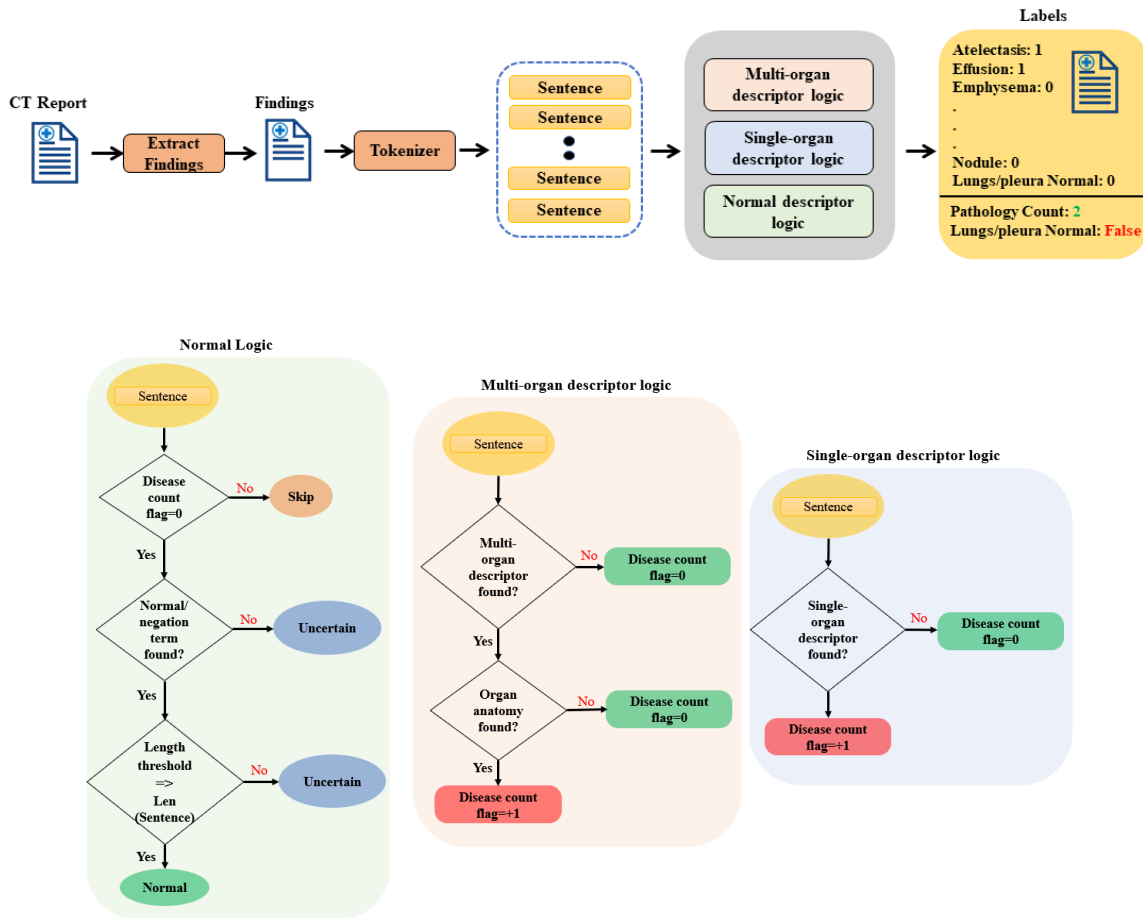


Fig. 4 Overview of the rule-based algorithm with normal, multi-organ, and single organ descriptor logics.

From the full set of 261,229 reports, the RBA classified a total of 165,659 reports from 74,944 subjects to extract labels for lungs/pleura, 96,532 reports from 50,086 subjects for liver/gallbladder, and 87,334 reports from 46,527 subjects for kidneys/ureters. Figure 5 displays the disease distribution by organ system. Reports were randomly divided by subject into subsets for training (70%), validation (15%), and testing (15%) the RNN model.

Since the RNN depends on labels generated by the RBA, we manually validated the quality of the RBA labels. From the above test set, a test subset of 2,158 (lungs/pleura=771, liver/gallbladder=652, kidneys/ureters=749) CT reports were randomly selected, and 2,875 labels (lungs/pleura=1,154, liver/gallbladder=787, kidneys/ureters=934) were manually obtained by a Master of Biomedical Science graduate with gross anatomy training (V.M.D.) who was supervised by a board-certified radiologist (G.D.R.). This reference set was used to compare performance of the final RBA against our previous versions.

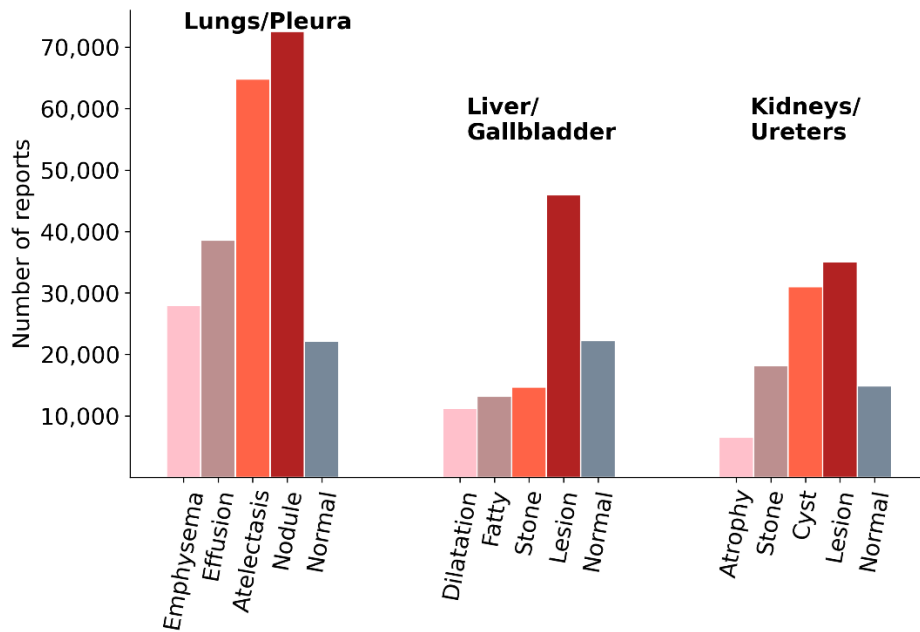


Fig 5. Frequency of reports for each disease and organ system.

2.3 Attention-Guided RNN and Training

The neural network (Fig. 1) used in this study consisted of an embeddings layer, Bidirectional Long-Short Term Memory (BiLSTM), attention mechanism, dense layer, and final classification layer (17, 18). The BiLSTM layer is composed of 200 units and produces a sequential output. It is followed up by a 0.2 dropout layer to prevent overfitting. The attention mechanism begins with a time-distributed dense layer, which receives a sequential 3-dimensional input (batch size,

maximum sequence length, 1), and computes the aggregation of each hidden state. Next, it is reshaped to 2-dimensional form (batch size, maximum sequence length) followed by softmax activation, which assigns weights to each hidden state to produce an attention vector. The dot product of the attention vector and sequential output of BiLSTM is the final output of the attention mechanism. It is then followed by dense and classification layers. Outcomes for each disease are non-mutually exclusive. Therefore, we used a weighted binary cross-entropy loss and model the outputs as independent Bernoulli distributions for each of the labels with sigmoid activation.

2.4 Pre-Training, Datasets, and Model Implementation

In this study, we compared the multi-label classification performance of two embedding approaches: with embeddings pretrained on the PubMed+MIMIC-III (19) dataset, and without pretrained embeddings (randomly initialized embedding layer). The embeddings of 200 dimensions were used in both experiments. Afterwards, we analyzed the effect of training data size on classification performance by incrementally increasing the number of training cases from 20%, 40%, 60%, 80%, or 100% of the total dataset. The models were trained for 50 epochs using a batch size of 512. The models corresponding to the minimum of the validation loss were selected as final. In this study we used Adam optimizer and a constant learning rate of 0.0001. The model was implemented using Python TensorFlow framework. Training duration was approximately 3 hours for all 6 models using 2 TITAN RTX GPUs. All models' weights and code will be made publicly available upon publication (<https://gitlab.oit.duke.edu/railabs/{to be announced}>).

3 Results

Table I displays the labeling accuracy and F-score of previously reported RBAs and the final RBA for the binary labels of each organ and disease. Performance was calculated based on the manually annotated test set of 2,158 CT reports with 2,875 labels. The performance of the final RBA was equal to or greater than both previously reported RBAs for all diseases, with accuracy ranging from 91% to 99% and F-score from 0.85 to 0.98.

Table I Comparison of classification performance between previously reported RBAs and the final RBA using the manually annotated test set. “# Pos” is the number of positive examples for that label in the test set, Acc=Accuracy. Boldface indicates the best performance for each disease.

Organ	Label	# Pos	Han <i>et al.</i> [10]		Faryna <i>et al.</i> [11]		Final RBA	
			Acc	F-Score	Acc	F-Score	Acc	F-Score
Lungs/ Pleura	Atelectasis	251	0.86	0.74	0.97	0.95	0.98	0.97
	Nodule	296	0.77	0.74	0.92	0.89	0.92	0.89
	Emphysema	193	0.82	0.45	0.98	0.96	0.99	0.98
	Effusion	205	0.82	0.53	0.84	0.58	0.98	0.97
	Normal	209	0.79	0.44	0.96	0.94	0.98	0.96
Liver/ Gallbladder	Stone	144	0.87	0.62	0.95	0.90	0.96	0.91
	Lesion	224	0.92	0.88	0.94	0.91	0.95	0.92
	Dilatation	87	0.86	0.10	0.90	0.70	0.98	0.92
	Fatty	166	0.97	0.94	0.98	0.96	0.98	0.96
	Normal	166	0.94	0.90	0.95	0.90	0.96	0.93
Kidneys /Ureters	Stone	174	0.91	0.82	0.93	0.85	0.93	0.85
	Atrophy	94	0.96	0.85	0.99	0.97	0.99	0.97
	Lesion	238	0.91	0.87	0.91	0.86	0.91	0.86
	Cyst	234	0.95	0.92	0.96	0.94	0.96	0.94
	Normal	194	0.94	0.89	0.96	0.92	0.96	0.92

Table II displays the classification performance of the attention-guided RNN with and without pre-trained embedding when applied to the test set of 23,411 reports for lungs/pleura; 13,402 reports for liver/gallbladder and 11,954 reports for kidneys/ureters. Pre-trained embedding outperformed the model trained with randomly initialized embedding for all organ systems and diseases.

Table II Performance of random v pre-trained embeddings using the test set of 48,758 (23,411 reports for lungs/pleura; 13,402 reports for liver/gallbladder and 11,954 reports for kidneys/ureters). # Pos represents the frequency of positive for that label. Values are reported as Area Under the Curve (AUC) with 95% confidence interval (CI). Bolded values represent an equivalent or increase in performance.

Organ	Label	# Pos	Random Embedding	Pre-trained
Lungs/ Pleura	Atelectasis	9329	0.9968 (0.9961-0.9974)	0.9973 (0.9967-0.9997)
	Nodule	10183	0.9913 (0.9904-0.9922)	0.9935 (0.9928-0.9943)
	Emphysema	3659	0.9972 (0.9963-0.9982)	0.9980 (0.9972-0.9987)
	Effusion	5625	0.9975 (0.9970-0.9980)	0.9984 (0.9980-0.9989)
	Normal	3110	0.9990 (0.9985-0.9995)	0.9990 (0.9982-0.9997)
Liver/ Gallbladder	Stone	1981	0.7849 (0.7739-0.7059)	0.9761 (0.9721-0.9801)
	Lesion	6463	0.9675 (0.9646-0.9700)	0.9946 (0.9936-0.9955)
	Dilatation	1497	0.8120 (0.8013-0.8228)	0.9926 (0.9906-0.9945)
	Fatty	1795	0.9984 (0.9851-0.9917)	0.9991 (0.9986-0.9996)
	Normal	3162	0.9745 (0.9716-0.9773)	0.9762 (0.9950-0.9974)
Kidneys/ Ureters	Stone	2548	0.9562 (0.9514-0.9609)	0.9792 (0.9764-0.9819)
	Atrophy	750	0.9523 (0.9436-0.9611)	0.9955 (0.9936-0.9973)
	Lesion	4817	0.9757 (0.9731-0.9783)	0.9900 (0.9886-0.9915)
	Cyst	4164	0.9862 (0.9843-0.9881)	0.9926 (0.9914-0.9939)
	Normal	2048	0.9909 (0.9890-0.9928)	0.9980 (0.9980-0.9992)

Fig. 6 shows examples of the output vectors produced by the attention mechanism for each organ system. Fig. 7 displays the classification performance of the attention-guided RNN with pre-trained embedding when different portions of training data are used. Fig. 7 (a) displays the number of reports used in the training dataset after randomly splitting in 20% increments for lungs/pleura, liver/gallbladder, kidneys/ureters. Fig. 7 (b) displays the classification performance after training with each increment. AUCs reached > 0.95 for all classes in each organ system when using the complete dataset in the pre-trained model. Although the performance tended to improve as more training samples were used, most labels showed a robust plateau such that performances were still within the confidence intervals for 100% of the data. The most notable drops in performance were classes with smaller sample size (e.g., stone and dilatation for liver/gallbladder and atrophy for kidneys/ureters).

Lungs/Pleura: Nodule

Text: unremarkable thyroid no enlarged supraclavicular or axillary lymph nodes multiple enlarged paratracheal ap window and subcarinal lymph nodes are present largest of which is in the subcarinal station measuring mm short axis series image a conglomerate of left paratracheal lymph nodes measures mm short axis series image a right paratracheal lymph node measures mm short axis series image an ap window lymph node measures mm short axis series image a top normal in size right hilar lymph node measures mm short axis series image a mildly enlarged left hilar lymph node measures mm short axis heart within normal limits in size without pericardial effusion moderate coronary artery calcifications ascending aorta within normal limits in size main pulmonary artery mildly enlarged to mm series image three vessel aortic arch mild calcific atherosclerosis of the thoracic aorta trachea and proximal bronchi are clear scattered mm or less nodules in the right lung are present series image a mm nodule abuts the left hemidiaphragm in the inferior left lower lobe series image no pleural effusion or pneumothorax visualized upper abdomen demonstrates nonspecific haziness of the upper abdominal mesentery associated with multiple subcentimeter lymph nodes this is nonspecific and may be seen in setting of mesenteric panniculitis apparent tiny low density lesions in the spleen may relate to phase of contrast degenerative changes of the thoracic spine mixed indeterminate lucent and sclerotic lesions in the t and t vertebral bodies are nonspecific in appearance

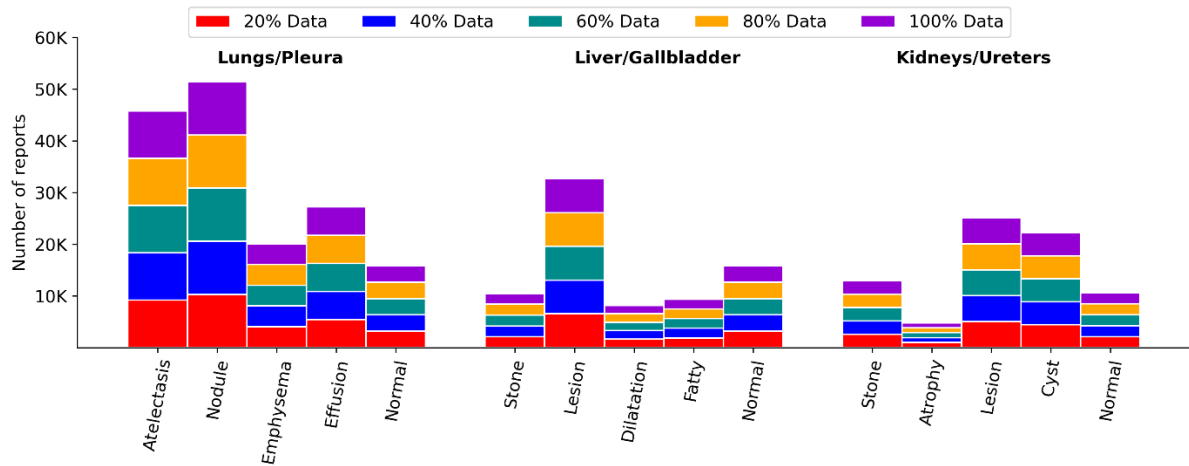
Liver/Gallbladder: Normal

Text: please see concurrent ct of the chest for findings above the diaphragm there is no evidence of focal hepatic mass or biliary obstruction the gallbladder pancreas spleen and adrenal glands are unremarkable there is no hydronephrosis multiple bilateral hypoenhancing renal lesions are too small to accurately characterize there has been significant enlargement of a periaortic lymph node measuring cm in short axis dimension previously cm series image tiny adjacent subcentimeter nodes are also increased in size there is no free fluid or free intraperitoneal gas there is no focal bowel wall thickening or evidence of intestinal obstruction scattered outside atherosclerosis in the abdominal aorta and its branches urinary bladder demonstrates no wall thickening or intraluminal filling defects there are no acute fractures or bony destructive lesions

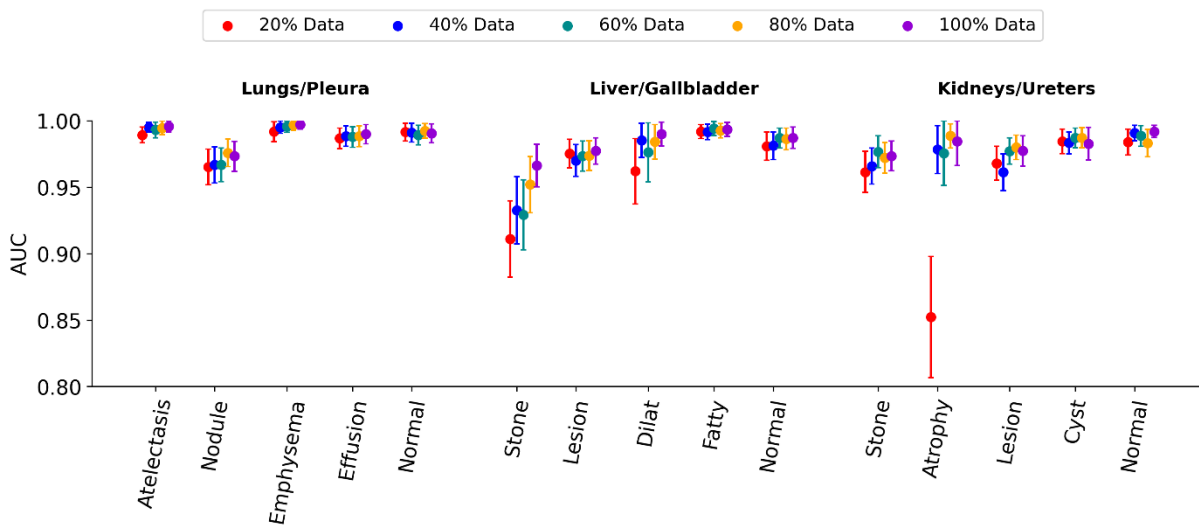
Kidneys/Ureters: Stone

Text: the lung bases are clear no pleural or pericardial effusion seen evaluation of the solid abdominal viscera is limited in the lack of ivcontrast the partially visualized liver gallbladder spleen pancreas and bilateral adrenal glands are normal in appearance there are bilateral nonobstructing renal calculi measuring up to mm on the left no hydronephrosis the kidneys are otherwise unremarkable in appearance there is a mm calculus at the left ureterovesicular junction series image the bowel is grossly unremarkable in appearance the urinary bladder and uterus are normal in appearance no pathologically enlarged inguinal pelvic mesenteric or retroperitoneal lymph nodes seen bone windows demonstrate no suspicious appearing osseous lesions

Fig 6. Example of attention vectors projected on reports for each organ system. Top panel shows a report positive for nodule in the lungs/pleura. Middle panel shows a normal report for liver/gallbladder. Bottom panel shows a report positive for stone in the kidneys/ureters.



(a)



(b)

Fig.7 Comparison of performance using different sizes of training data in the pretrained model for the lungs/pleura, liver/gallbladder, kidneys/ureters. (a) Number of reports randomly split in 20%, 40%, 60%, 80% and 100% of total training dataset for each disease by organ system (b) Performance of models on test-set trained with randomly split 20%, 40%, 60%, 80% and 100% training data for each disease by organ system.

4 Discussion

Although deep learning-based disease classification algorithms have achieved exceptional accuracy, they often suffer from limited diversity of diseases and organ systems. This narrow scope is largely due to inadequate amounts of curated CT data where human-annotation efforts are required. As an alternative, the work described here sought to develop a high-throughput, multi-disease label extractor for body CT reports that was broad in scope and could be easily adapted to new diseases. As the foundation of our NLP algorithm, we developed an RBA that utilized simple rules to extract precise labels from radiology reports with 91-99% accuracy for all four diseases or normal across all three organ systems.

However, the RBA alone cannot provide labels for our entire dataset because radiology reports often contain variability in writing, grammar, and even variation in descriptors for the same disease between radiologists (20). To overcome this obstacle, we demonstrated that an attention-guided RNN can be trained using RBA-annotated reports to learn salient semantic features and generalize beyond simple rules or keywords to encompass more reports. Our final disease classification pipeline performed with an AUC of > 0.96 for all diseases and organ systems. Recent works investigating deep learning-based radiology report annotation have achieved similar performances, although the majority are limited to a specific disease or organ system (21). Examples include classification of pulmonary emboli in thoracic CT reports using an attention-guided RNN with AUC ranging from 0.93-0.99 (22), multilabel annotation of mammography reports using a combined RNN and convolutional network (CNN) with a keyword accuracy of 0.96 (23), and identification of femur fractures in multiple types of radiograph reports using a CNN with an F1 score of 0.97 (24).

Further inspired by the recent wide application of deep learning-based methods in different clinical NLP tasks (10, 25-31) and effective application of word embedding (32-34), we also experimented using a multi-label disease classifier with pre-trained embedding and randomly initialized embedding layers. As expected, the attention-guided RNN with pretrained embedding outperformed the randomly initialized model in all classes across all organ systems. Additionally, we observed that performance improved steadily with increasing number of cases. The lower frequency classes seemed to be affected greatly compared to classes having high frequency, as exemplified by atrophic kidneys where performance experienced a significant drop at around 500 cases (20% of total available cases) for training.

This study demonstrated that a body CT dataset will be dominated by two types of exams: chest and abdomen-pelvis CTs. In many reports, one or more of the three organ systems were out of view and not mentioned at all by the radiologist. For example, if a chest CT did not mention the kidneys, that would be labeled as uncertain by our RBA. However, in specific studies such as abdomen-pelvis CT, large organs such as the lung were often still described even if they were not completely visible e.g., “Limited view of the lung bases appear clear.” This short sentence would satisfy the logic of the RBA to label the report appropriately as normal for the lungs.

There are several limitations to this study. As a general limitation of RBA techniques, it was not possible to provide disease labels for all reports within our dataset. This was often because each sentence did not satisfy the pre-defined, strict rules. While the addition of pre-defined organ or disease keywords can mitigate this effect, but this is a tedious and potentially limitless task. For this initial demonstration, we limited the analysis to a relatively narrow group of organs and diseases, and this scope should be expanded in future work. Additionally, unlike when radiologists annotate images manually, the labels derived from reports tend to describe all or much of an organ

system (e.g., “bibasilar atelectasis”), or in some cases provide limited disease extent and location (e.g., “nodule measuring 1.8 x 2.1 cm on series 2 image 60”). Furthermore, our dataset suffered from notable class imbalance, including a low prevalence of normal cases as well as multi-fold differences between diseases, although this represented the natural prevalence within our study population. Finally, the dataset comes from a single health system, which comprises multiple hospitals but may share similarities in the practice patterns for radiologists.

Overall, the disease labeling pipeline described here offers numerous advantages. By using deep learning-based NLP, our algorithm was able to generalize beyond pre-defined rules and label a vast and heterogenous dataset as positive for one or more diseases or normal. To the best of our knowledge, this was a first attempt in using RBA-extracted labels to train an attention-guided RNN to annotate a diverse set of diseases in a hospital-scale dataset of body CT reports. Ultimately, the work described here seeks to facilitate future research in image-based disease classification algorithms by providing a general framework for labeling vast amounts of hospital-scale data in a manner that is both cost and time efficient.

Appendix 1. Dictionary structure used in this study.

	Lungs/Pleura	Liver/Gallbladder	Kidneys/Ureters
Organ Anatomy	lung, pulmonary, lower upper middle lobe, centrilobular, perifissural, left right base, bases, basilar, bronch-, trachea, airspace, airway.	liver, hepatic, hepatogallbladder, gall bladder, biliary, bile, left right caudate quadrate lobe.	kidney, renal, nephr-, ureter, cort-, medul-, caliectasis, UVJ
Single-organ Disease descriptors	pneumothorax, emphysema, pneumoni-, ground glass, aspiration, bronchiectasis, atelecta-, embol-, air trapping, pleural effusion, pneumonectomy.	steatosis, cirrho-, cholecystectomy, gallstone, cholelithiasis.	hydronephrosis, hydroureter, nephrectomy, pelvicaliectasis, uropathy, ureterectasis, nephrolithiasis.
Multi-organ Disease Descriptors	mass, opaci-, calcul-, stone, scar, metas-, malignan-, cancer, tumor, neoplasm, lithiasis, atroph, recurren-, hyperenhanc-, hypoenhanc-, aneurysm, lesion, nodule, nodular, calcifi-, opacit-, effusion, resect, thromb-, infect, infarct, inflam-, fluid, consolidat-, degenerative, dissect, collaps-, fissure, edema, cyst, focus, angioma, spiculated, architectural distortion, lytic, pathologic, defect, hernia, biops-, encasement, fibroid, hemorrhage, multilocul, distension, stricture, obstructi-, hypodens-, hyperdens-, hypoattenuat-, hyperattenuat-, necrosis, irregular, ectasia, destructi-, dilat-, granuloma, enlarged, abscess, stent, fatty infiltr-, stenosis, delay, carcinoma, adenoma, atrophy, hemangioma, density, surgically absent.		
Negation	no, non, other, not, none, without, rather, negative, with regards to, however is no, are no, no evidence, noevidence, limited exam for the evaluation.		
Other	acute, new, size, contour, attenuation, caliber, however, morphological.		
Normal	Normal, unremarkable, negative exam, patent, clear, no abnormalit-, without abnormalit-.		

References

1. E. Pons et al., "Natural language processing in radiology: a systematic review," *Radiology* **279**(2), 329-343 (2016).
2. K. J. Dreyer et al., "Application of recently developed computer algorithm for automatic classification of unstructured radiology reports: validation study," *Radiology* **234**(2), 323-329 (2005).
3. I. Solti et al., "Automated classification of radiology reports for acute lung injury: comparison of keyword and machine learning based natural language processing approaches," *2009 IEEE International Conference on Bioinformatics and Biomedicine Workshop* 314-319 (2009).
4. B. Percha et al., "Automatic classification of mammography reports by BI-RADS breast tissue composition class," *J. Am. Med. Inform. Assoc.* **19**(5), 913-916 (2012).
5. X. Wang et al., "ChestX-Ray8: Hospital-Scale Chest X-Ray Database and Benchmarks on Weakly-Supervised Classification and Localization of Common Thorax Diseases," in *2017 IEEE Conference on Computer Vision and Pattern Recognition (CVPR)*, pp. 3462-3471 (2017).
6. R. L. Draelos et al., "Machine-learning-based multiple abnormality prediction with large-scale chest computed tomography volumes," *Med. Image Anal.* **67**(101857) (2021).
7. D. Ganeshan et al., "Structured reporting in radiology," *Acad. Radiol.* **25**(1), 66-73 (2018).
8. L. Deng, and Y. Liu, *Deep learning in natural language processing*, Springer (2018).
9. D. Bahdanau, K. Cho, and Y. Bengio, "Neural machine translation by jointly learning to align and translate," *arXiv preprint arXiv:1409.0473* (2014).
10. J. M. Steinkamp et al., "Automated Organ-Level Classification of Free-Text Pathology Reports to Support a Radiology Follow-up Tracking Engine," *Radiology: Artificial Intelligence* **1**(5), e180052 (2019).
11. J. Yuan, H. Zhu, and A. Tahmasebi, "Classification of Pulmonary Nodular Findings based on Characterization of Change using Radiology Reports," *AMIA Jt Summits Transl Sci Proc* **2019**(285-294) (2019).
12. C. Raffel, and D. P. Ellis, "Feed-forward networks with attention can solve some long-term memory problems," *arXiv preprint arXiv:1512.08756* (2015).
13. Y. Wang et al., "Attention-based LSTM for aspect-level sentiment classification," *Proceedings of the 2016 conference on empirical methods in natural language processing* 606-615 (2016).
14. S. Han et al., "Classifying abnormalities in computed tomography radiology reports with rule-based and natural language processing models," in *Medical Imaging 2019: Computer-Aided Diagnosis* (2019).
15. K. Faryna et al., "Attention-guided classification of abnormalities in semi-structured computed tomography reports," in *Medical Imaging 2020: Computer-Aided Diagnosis* (2020).
16. H. C. Wu et al., "Interpreting TF-IDF term weights as making relevance decisions," *ACM Trans. Inf. Syst.* **26**(3), Article 13 (2008).
17. S. Hochreiter, and J. Schmidhuber, "Long Short-Term Memory," *Neural Comput.* **9**(8), 1735-1780 (1997).

18. Q. Zhou, and H. Wu, "NLP at IEST 2018: BiLSTM-attention and LSTM-attention via soft voting in emotion classification," *Proceedings of the 9th Workshop on Computational Approaches to Subjectivity, Sentiment and Social Media Analysis* 189-194 (2018).
19. Y. Zhang et al., "BioWordVec, improving biomedical word embeddings with subword information and MeSH," *Scientific Data* **6**(1), 52 (2019).
20. A. Brady et al., "Discrepancy and error in radiology: concepts, causes and consequences," *Ulster Med J* **81**(1), 3-9 (2012).
21. V. Sorin et al., "Deep learning for natural language processing in radiology—fundamentals and a systematic review," *Journal of the American College of Radiology* **17**(5), 639-648 (2020).
22. I. Banerjee et al., "Comparative effectiveness of convolutional neural network (CNN) and recurrent neural network (RNN) architectures for radiology text report classification," *Artif. Intell. Med.* **97**(79-88 (2019).
23. R. G. Short et al., "Comprehensive word-level classification of screening mammography reports using a neural network sequence labeling approach," *J. Digit. Imaging* **32**(5), 685-692 (2019).
24. Y. Wang et al., "A clinical text classification paradigm using weak supervision and deep representation," *BMC Med. Inform. Decis. Mak.* **19**(1), 1-13 (2019).
25. W. H. Weng et al., "Medical subdomain classification of clinical notes using a machine learning-based natural language processing approach," *BMC Med Inform Decis Mak* **17**(1), 155 (2017).
26. A. Spandorfer et al., "Deep learning to convert unstructured CT pulmonary angiography reports into structured reports," *Eur Radiol Exp* **3**(1), 37 (2019).
27. H.-C. Shin et al., "Learning to Read Chest X-Rays: Recurrent Neural Cascade Model for Automated Image Annotation," in *2016 IEEE Conference on Computer Vision and Pattern Recognition (CVPR)*, pp. 2497-2506 (2016).
28. J. Laserson et al., "TextRay: Mining Clinical Reports to Gain a Broad Understanding of Chest X-Rays," in *Medical Image Computing and Computer Assisted Intervention – MICCAI 2018*, pp. 553-561 (2018).
29. C. Kim et al., "Natural language processing and machine learning algorithm to identify brain MRI reports with acute ischemic stroke," *PLoS One* **14**(2), e0212778 (2019).
30. E. Choi et al., "Using recurrent neural network models for early detection of heart failure onset," *J Am Med Inform Assoc* **24**(2), 361-370 (2017).
31. M. J. Willeminck et al., "Preparing Medical Imaging Data for Machine Learning," *Radiology* **295**(1), 4-15 (2020).
32. Y. Zhang et al., "Drug-drug interaction extraction via hierarchical RNNs on sequence and shortest dependency paths," *Bioinformatics* **34**(5), 828-835 (2018).
33. D. Tang et al., "Learning sentiment-specific word embedding for twitter sentiment classification," *Proceedings of the 52nd Annual Meeting of the Association for Computational Linguistics (Volume 1: Long Papers)* 1555-1565 (2014).
34. Y. Wang et al., "A comparison of word embeddings for the biomedical natural language processing," *J Biomed Inform* **87**(12-20 (2018).